

# Fusion of Single and Integral Multispectral Aerial Images

Mohamed Youssef<sup>1</sup> and Oliver Bimber<sup>2, \*</sup>

<sup>1</sup> Johannes Kepler University; mohamed.youssef@jku.at

<sup>2</sup> Johannes Kepler University; oliver.bimber@jku.at

\* Correspondence: oliver.bimber@jku.at; Tel.: +43-732-2468-6631

**Abstract:** We present a novel hybrid (model- and learning-based) architecture for fusing the most significant features from conventional aerial images and integral aerial images that result from synthetic aperture sensing for removing occlusion caused by dense vegetation. It combines the environment's spatial references with features of unoccluded targets. Our method out-beats the state-of-the-art, does not require manually tuned parameters, can be extended to an arbitrary number and combinations of spectral channels, and is reconfigurable to address different use-cases.

**Keywords:** image fusion; aerial imaging; multispectral, synthetic aperture sensing, Airborne Optical Sectioning, occlusion removal

---

## 1. Introduction

Occlusion caused by dense vegetation, such as forest, represents a fundamental problem for many applications that apply aerial imaging. These include, search and rescue, wildfire detection, wildlife observation, surveillance, forestry, agriculture, and archology. With Airborne Optical Sectioning (AOS) [1-17] we have introduced a synthetic aperture imaging technique that removes occlusion in aerial images in real-time (cf. Fig. 1a-d). It computationally registers and integrates multiple (single) images captured with conventional camera optics at different drone positions to an integral image that mimics a wide (several meters) synthetic aperture camera. Thereby, the area in which the single images are sampled represents the size of the synthetic aperture. Image registration and integration depend both on the camera poses of where the single images have been recorded and on a given focal surface (e.g., a defined plane or a registered digital elevation model of the ground surface). The resulting integral images have an extremely shallow depth of field. Because of this, all targets located on the focal surface appear sharp and unoccluded while occluders not located on the focal surface appear severely defocused. In fact, the blur signal of the occluders is spread widely over the integral image, which suppresses their contribution. High spatial resolution, real-time processing capabilities, and wavelength independents are the main advantages of AOS over alternatives, such as light detecting and ranging (LiDAR) or synthetic aperture radar (SAR). AOS can be applied to images captured in the visible, the near-infrared, or the far-infrared spectrum, and processing is in the range of milliseconds.

One main limitation of the integral images is their lack of spatial references as the surrounding environment's details are suppressed in the shallow depth of field. In this article we propose a novel hybrid (model- and learning-based) architecture for fusing the most significant information from single and integral aerial images into one composite image (cf. Figs. 1e-h). This composite image combines the environment's spatial references provided by single images (in some cases also by integral images) with features of the unoccluded targets provided by integral images. Our method out-beats the state-of-the-art, does not require manually tuned parameters, can be extended to an arbitrary number

---

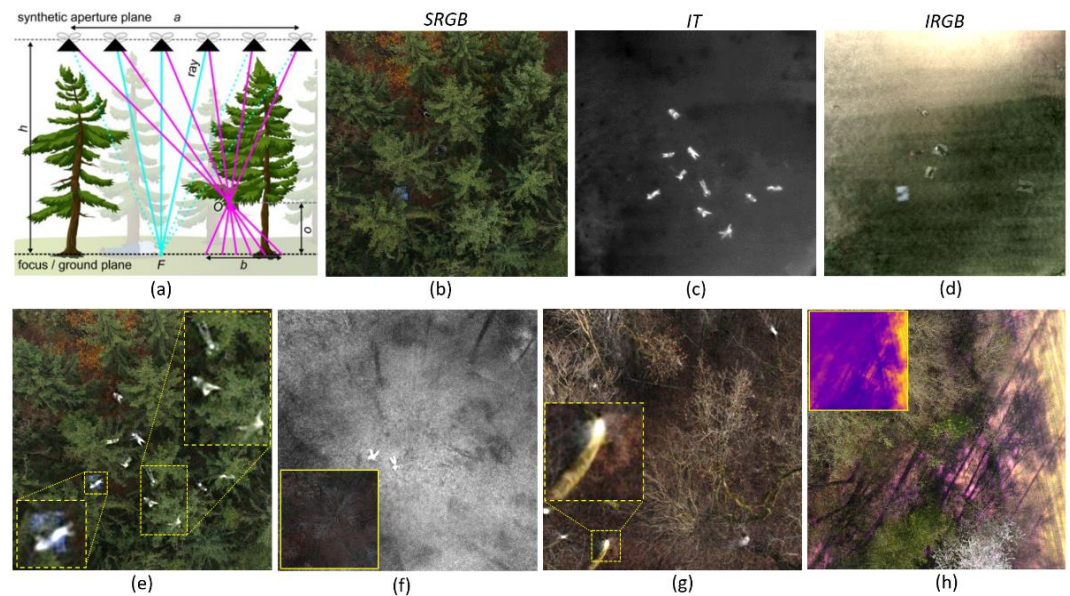


**Figure 1.** Airborne Optical Sectioning (AOS) principle (a): Registering and integrating multiple images captured along a synthetic aperture of size  $a$  while computationally focusing on focal plane  $F$  at distance  $h$  will defocus occluders  $O$  at distance  $o$  from  $F$  (with a point-spread of  $b$ ) while focusing targets on  $F$ . Single RGB image, SRGB (b); integral thermal image, IT (c); and integral RGB image, IRGB (d) of dense forest captured with a square synthetic aperture area ( $30\text{m} \times 30\text{m}$ ) with  $1\text{m} \times 3\text{m}$  dense sampling while computationally focusing on the forest ground. All images show the same scene, at the same time, from the same pose. (e) Fused result from (b-d). Close-ups in dashed boxes. (f) Fusion of IT and IRGB under dark light conditions – increasing exposure through integration. Original SRGB image in solid box. (g) SRGB and IT fusion of sparse forest – highlighting the bottoms of tree trunks in the thermal channel. Close-up in dashed box. (h) SRGB and color-coded IT fusion – revealing hot ground patches in the IT channel. Color-coded IT image in solid boxes.

and combinations of spectral channels, and is reconfigurable to address different use-cases.

Image fusion, especially for recordings in the infrared and the visible spectral ranges, has become an active research field in recent years. Feature extraction and the fusion strategy itself are two main components of such methods. Multi-scale transform-based approaches [18–21] split images into multiple scales for the analysis of both: fine and coarse features. Low-rank-based methods [22,23] decompose the image matrix into low-rank and sparse representations. Such model-based approaches often require a lot of computation resources and extensive manual adjustments. In [24], a hybrid concept is followed which first extracts features using a model-based approach, and then feeds these features as input to a learning-based approach (i.e., a pretrained neural network). Usually, convolutional neural networks (CNNs) or generative adversarial networks (GANs) are architectures of choice for image fusion today. CNNs are used to extract local and global features and for generating the fused image [25–28]. However, despite their remarkable fusion performance over model-based approaches, deeper networks often lose important details due to stacking a series of pooled convolution layers. Transformer architectures [30–33] can overcome this by extracting complementary features from the input images. With GANs the problem of a limited amount of ground-truth data for infrared-visible image fusion can be overcome. The GAN learning scheme [34] depends on the generator and discriminator, and such architectures discriminate between the generated fused image and the input images [35]. However, using only one discriminator may lead to networks being biased towards favoring either the generated fused images or the input images. Therefore, dual discriminators were adopted [36–37] to ensure high quality fusion results.

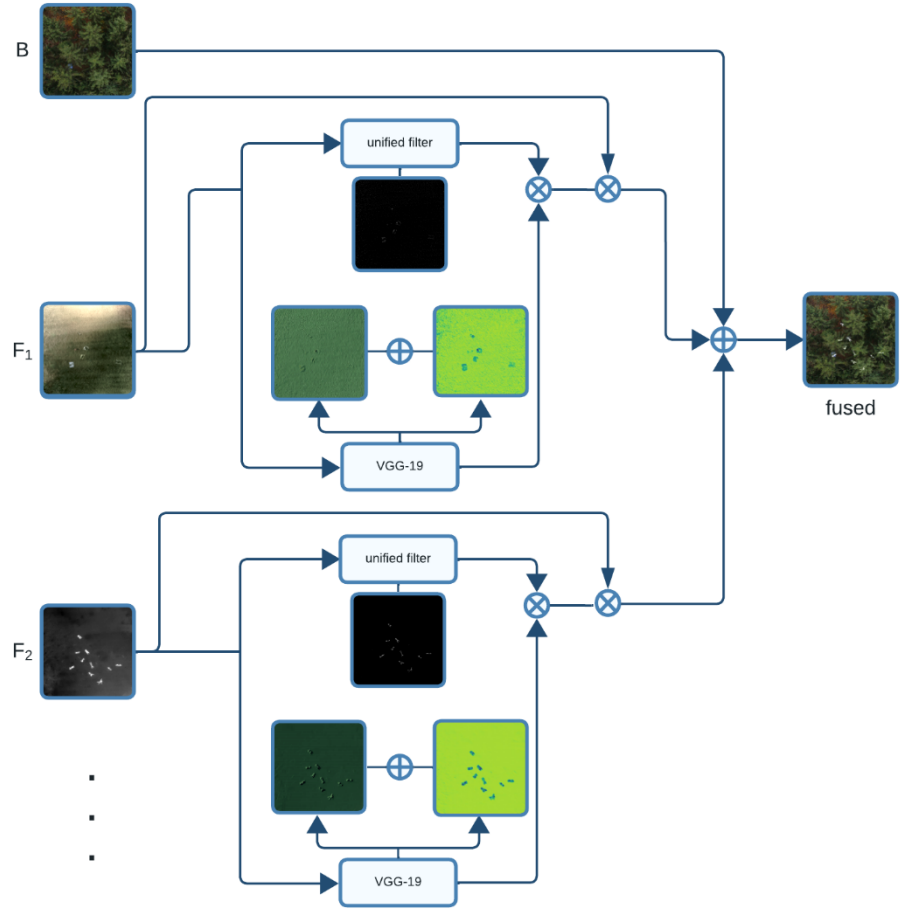


**Figure 2.** Proposed hybrid fusion architecture. Multiple input channels (one basis channel that remains unmodified and provides spatial references, and an arbitrary number of additional channels from which salient features are extracted) are fused to one composite image. Each feature channel applies multiple model-based and learning-based feature extractors (unified filters and VGG-layers in our case).

## 2. Materials and Methods

Our proposed architecture is depicted in Figure 2. It has  $f + 1$  input channels, whereby one channel takes a basis image ( $B$ ) that remains unmodified to provide spatial references. The other channels take images ( $F_1 \dots F_f$ ) from which features need to be extracted and fused with the basis image. Depending on the use-case, the input to the channels can vary. For instance, single RGB (SRGB) images were used for the basis channel in Figs. 1e,g,h, while integral thermal (IT) images were used instead in Fig. 1f; raw integral images were used in the feature channels in Figs. 1e-g, while color-coded IT was used instead in Fig. 1h. Integral RGB (IRGB) and SRGB images were used in the feature channels. Note, that the fusion process is the same for more than two feature channels.

As shown in Fig. 2, each  $F_n$ -branch splits into two parallel branches for feature extraction: one with a unified filter [38] for model-based feature extraction and one with the pretrained very deep convolutional network, VGG-19 [39], for learning-based feature extraction.

The unified filter determines the high detail part ( $H_n$ ) of the input channel ( $F_n$ ) as follows:

$$H_n = F_n - \arg \min_{H_n} \|F_n - H_n\|_2^2 + \lambda (\|g_x * H_n\|_2^2 + \|g_y * H_n\|_2^2) , \quad (1)$$

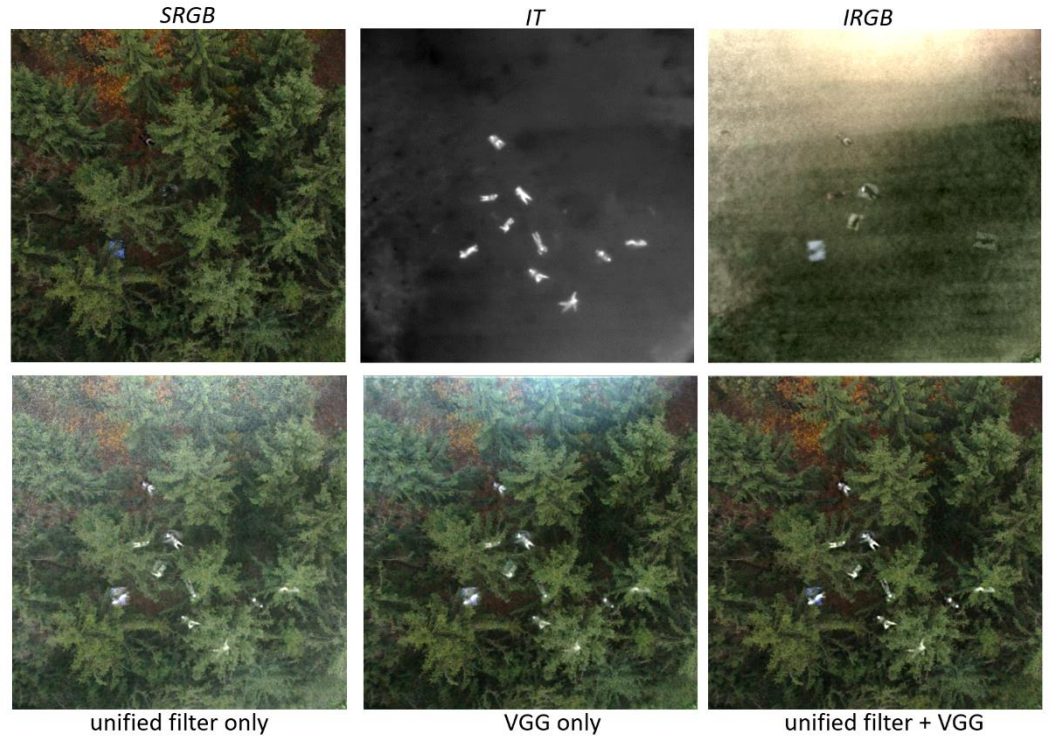


**Figure 3.** Comparison of fusion results with unified filter only, VGG only, and the combination of unified filter and VGG. Only in the latter case background noise and sampling artefacts can be removed efficiently and essential target features are enhanced. The input images (SRGB, IT, IRGB) show the same scene, at the same time, from the same pose.

where we always used the default of  $\lambda = 5$ , as optimized in [24], and  $g_x = [-1 \ 1]$  and  $g_y = [-1 \ 1]^T$  are horizontal and vertical gradient operators, respectively.

The pretrained VGG-19 network architecture shows remarkable results in feature extraction which is usually applied for classification tasks. Consider  $\phi_n^i$  indicates the features map extracted from  $n$ -th channel in the  $i$ -th VGG-19 layer:

$$\phi_n^i = \Phi_i(F_n), \quad (2)$$

where  $\Phi_i(\cdot)$  denotes a  $i$ -th layer. Deeper layers in VGG detect high-level features, while lower-level layers detect abstract features such as edges and colors. We decided to use only the first two layers (i.e.,  $i \in \{1, 2\}$  – which represents *relu\_1\_1* and *relu\_2\_1*, respectively), as we are more interested in the abstract, low-level salient features from  $F_n$  rather than its high-level features.

After determining the features  $\phi_n^i$ , an activity level map  $A_n^i$  is calculated by the  $l_1$  – norm:

$$A_n^i = \sum_x \sum_y \sum_c |\phi_n^i(x, y, c)|, \quad i \in \{1, 2\}. \quad (3)$$

Afterwards, weighted average maps are calculated by the soft-max operator:

$$W_n = \frac{A_n^i}{\sum_{j=1}^J A_n^j}, \quad i \in \{1, 2\}, \quad (4)$$

where  $(x, y)$  is the position in the feature map and  $c$  is the channel number.

The initially features mask is calculated as follows:

$$FM_n(x, y) = \sum_{n=1}^f W_n(x, y) \times H_n(x, y), \quad (5)$$

and the final feature map is then:

$$G_n(x, y) = FM_n(x, y) \times F_n(x, y). \quad (6)$$

Finally, the feature maps from all feature channels are fused with the basis channel:

$$fused(x, y) = B(x, y) + \sum_{n=1}^f G_n(x, y). \quad (7)$$

Our goal with this architecture is to preserve the salient information from all input channels. This, however, can only be achieved if multiple feature extractors (unified filters and VGG in our case) are combined. Applying them independently fails in removing background noise and in enhancing the essential target features, as demonstrated in Fig. 3.

### 3. Results

Figure 4 presents a visual comparison of our approach with several state-of-the-art image fusion techniques for various scenes and use-cases: (c) is an open field without occlusion, (a,b,d,e,f) are forest patches with different types of vegetation and densities, (a,b,c,f) show people lying on the ground, (d,e) are empty forests. Useful features to be fused are contained SRGB, IT, and ITGB for (a,b,f), in IT and IRGB for (c), and in SRGB and IT (d,e). The IT image is color coded in (e,f). For all integral images (IT and IRGB) the synthetic focal plane was set to the ground surface. Note, that a quantitative comparison is not possible, as a ground truth result does not exist.

While some of the evaluated state-of-the-art fusion methods support only two input channels [27, 30–32], [24] scales to multiple channels. In cases only two channels are supported but three channels could be used, we selected SRGB and IT. In cases only grayscale input is supported [30–31] but color input is provided, we convert color images to grayscale.

The poor quality of simple image processing, such as alpha blending with an equal contribution per input channel, clearly calls for more sophisticated approaches that are capable of extracting and fusing the essential image features. The only image fusion method that is scalable to multiple (more than two) input channels [24] does not provide significantly better results than alpha blending in our experiments. The reason for this is that, in spite of using also VGG-19 for feature extraction, the final fusion process relies on image averaging.

All newer methods support only two input channels and still fail to differentiate between essential image features and other high gradient features that are considered unimportant (e.g., noise and sampling artefacts). Consequently, fused results appear unnatural and do not reflect properly the salient image features and details of the original input channels. Although [31] uses transformers for global feature extraction, it fails to extract the local features correctly due to the lack of sufficient correlation between neighboring pixels. In [27], a multi-model was trained for fusion and detection tasks that mutually shares learned features between the two models (i.e., fusion and detection). It struggles in generalizing to our particular fusion problem, and fails to preserve salient information in our data as it is trained on a very different benchmark dataset [40] that is specialized to infrared and visible fusion for object detection. The work in [30] can't accurately estimate complementary information between input images if target objects are discriminative in both images. The architecture in [32] fails in generating the saliency mask, as it was only trained on a small dataset [41] for extracting the mask, which leads to a poor fusion output at the end.

Our approach preserves the natural appearance of the input channels while effectively merging their essential features. It is scalable to an arbitrary number of input channels, does not require manually tuned parameters, supports color as well as grayscale input, and is reconfigurable to address different use-cases.

On a 3.2 GHz Intel Core CPU with 24 GB RAM and GPU GTX 1060 6 GB, our python implementation of the proposed fusion architecture requires (for 512×512px input images), approx. 1.2 s per feature channel plus 10 ms for fusing feature channel with basis channel.

#### 4. Discussion and Conclusion

An adequate fusion of the most significant information from multiple input channels is essential for many aerial imaging tasks. While multispectral recordings reveal features in various spectral ranges, synthetic aperture sensing makes occluded features visible. Our proposed method effectively fuses all of these features into one composite image which provides important spatial reference queues. It is extendable to an arbitrary number of input channels, easy to use as it does not require manually tuned parameters, and reconfigurable to address different use-cases. Such use-cases include search and rescue, soil moisture analysis, wildfire detection and monitoring, observation and tracking of wildlife, surveillance, border control, and others. Occlusion caused by dense vegetation is often a limiting factor for these tasks.

In future, we want to explore if extending our architecture by more than two feature extractor branches per feature channel further improves results, and how to achieve real-time performance.

**Supplementary Materials:** The source code and sample images can be downloaded at: <https://github.com/JKU-ICG/AOS/>.

**Author Contributions:** Conceptualization, O.B.; methodology, O.B. and M.Y.; software, M.Y.; validation, O.B. and M.Y.; formal analysis, O.B. and M.Y.; investigation, O.B. and M.Y.; resources, M.Y.; data curation, O.B. and M.Y.; writing—original draft preparation, O.B. and M.Y.; writing—review and editing, O.B. and M.Y.; visualization, O.B. and M.Y.; supervision, O.B.; project administration, O.B.; funding acquisition, O.B. All authors have read and agreed to the published version of the manuscript.

**Funding:** This research was funded by the Austrian Science Fund (FWF) and German Research Foundation (DFG) under grant numbers P32185-NBL and I 6046-N, as well as by the State of Upper Austria and the Austrian Federal Ministry of Education, Science and Research via the LIT-Linz Institute of Technology under grant number LIT2019-8-SEE114.

**Data Availability Statement:** The data presented in this study are openly available in Zenodo at DOI 10.5281/zenodo.10210035, reference number [10210035].

**Conflicts of Interest:** The authors declare no conflict of interest.



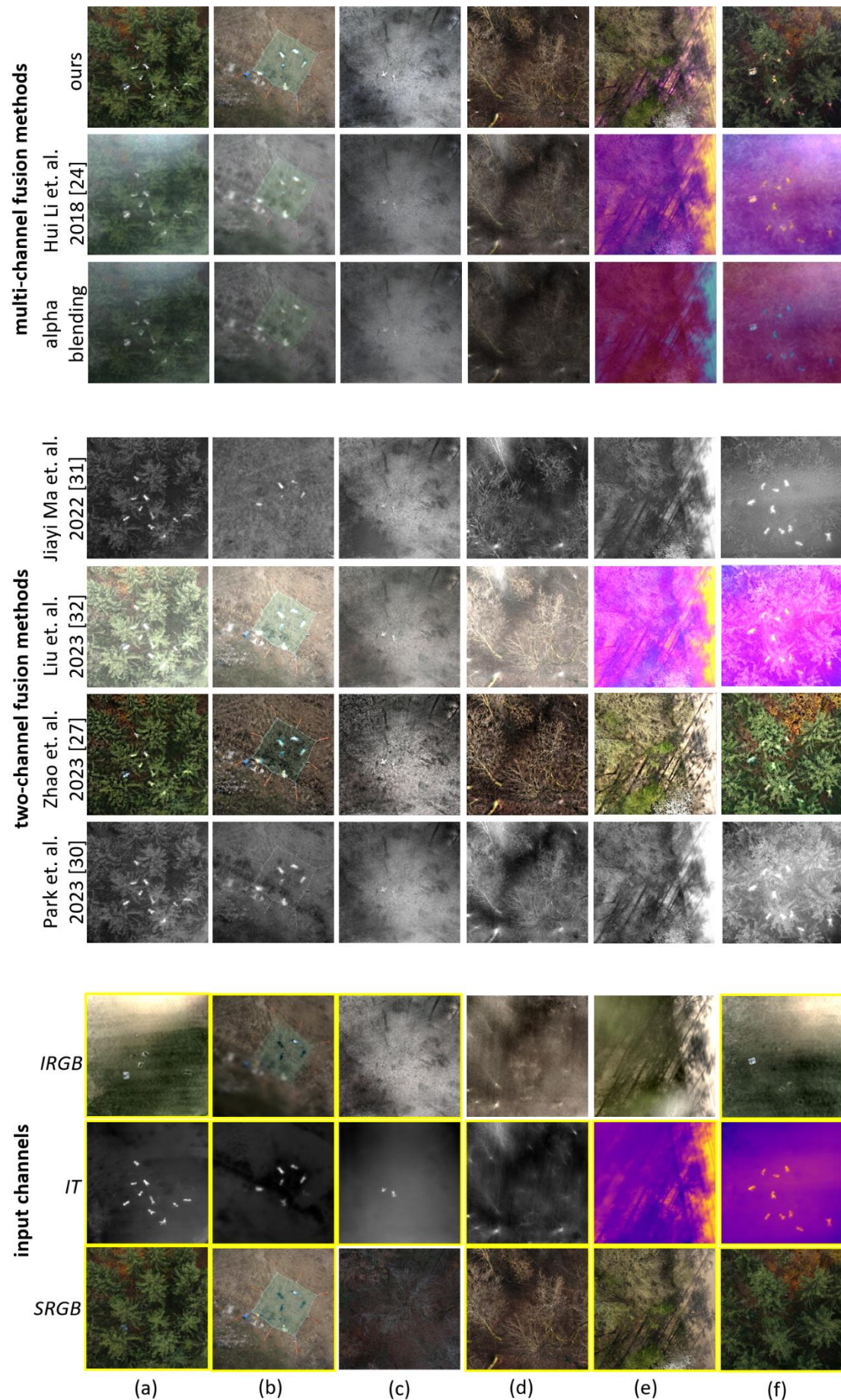


**Figure 4.** Comparison of our approach with several state-of-the-art two- and multi-channel image fusion techniques for various scenes and use-cases. Input channels (*SRGB*, *IT*, *IRGB*) indicated with yellow solid box contain useful features to be fused. They show the same scene, at the same time, from the same pose. The data used for our experiments and details on how it was recorded can be found in [9]. All images, except for (c), have been brightness increased by 25% for better visibility.

## References

1. Kurmi, I.; Schedl, D.C.; Bimber, O. Airborne Optical Sectioning. *Journal of Imaging* **2018**, *4*, 102, doi:[10.3390/jimaging4080102](https://doi.org/10.3390/jimaging4080102).
2. Bimber, O.; Kurmi, I.; Schedl, D.C. Synthetic Aperture Imaging With Drones. *IEEE Computer Graphics and Applications* **2019**, *39*, 8–15, doi:[10.1109/MCG.2019.2896024](https://doi.org/10.1109/MCG.2019.2896024).
3. Kurmi, I.; Schedl, D.C.; Bimber, O. A Statistical View on Synthetic Aperture Imaging for Occlusion Removal. *IEEE Sensors Journal* **2019**, *19*, 9374–9383, doi:[10.1109/JSEN.2019.2922731](https://doi.org/10.1109/JSEN.2019.2922731).
4. Kurmi, I.; Schedl, D.C.; Bimber, O. Thermal Airborne Optical Sectioning. *Remote Sensing* **2019**, *11*, 1668, doi:[10.3390/rs11141668](https://doi.org/10.3390/rs11141668).
5. Kurmi, I.; Schedl, D.C.; Bimber, O. Fast Automatic Visibility Optimization for Thermal Synthetic Aperture Visualization. *IEEE Geoscience and Remote Sensing Letters* **2021**, *18*, 836–840, doi:[10.1109/LGRS.2020.2987471](https://doi.org/10.1109/LGRS.2020.2987471).
6. Kurmi, I.; Schedl, D.C.; Bimber, O. Pose Error Reduction for Focus Enhancement in Thermal Synthetic Aperture Visualization. *IEEE Geoscience and Remote Sensing Letters* **2022**, *19*, 1–5, doi:[10.1109/LGRS.2021.3051718](https://doi.org/10.1109/LGRS.2021.3051718).
7. Seits, F.; Kurmi, I.; Nathan, R.J.A.A.; Ortner, R.; Bimber, O. On the Role of Field of View for Occlusion Removal with Airborne Optical Sectioning. *arXiv* **2022**, *arXiv preprint arXiv:2204.13371*.
8. Schedl, D.C.; Kurmi, I.; Bimber, O. Airborne Optical Sectioning for Nesting Observation. *Sci Rep* **2020**, *10*, 7254, doi:[10.1038/s41598-020-63317-9](https://doi.org/10.1038/s41598-020-63317-9).
9. Schedl, D.C.; Kurmi, I.; Bimber, O. Search and Rescue with Airborne Optical Sectioning. *Nat Mach Intell* **2020**, *2*, 783–790, doi:[10.1038/s42256-020-00261-3](https://doi.org/10.1038/s42256-020-00261-3).
10. Schedl, D.C.; Kurmi, I.; Bimber, O. An Autonomous Drone for Search and Rescue in Forests Using Airborne Optical Sectioning. *Science Robotics* **2021**, *6*, eabg1188, doi:[10.1126/scirobotics.abg1188](https://doi.org/10.1126/scirobotics.abg1188).
11. Kurmi, I.; Schedl, D.C.; Bimber, O. Combined Person Classification with Airborne Optical Sectioning. *Sci Rep* **2022**, *12*, 3804, doi:[10.1038/s41598-022-07733-z](https://doi.org/10.1038/s41598-022-07733-z).
12. Ortner, R.; Kurmi, I.; Bimber, O. Acceleration-Aware Path Planning with Waypoints. *Drones* **2021**, *5*, 143, doi:[10.3390/drones5040143](https://doi.org/10.3390/drones5040143).
13. Nathan, R.J.A.A.; Kurmi, I.; Schedl, D.C.; Bimber, O. Through-Foliage Tracking with Airborne Optical Sectioning. *Journal of Remote Sensing* **2022**, *2022*, doi:[10.34133/2022/9812765](https://doi.org/10.34133/2022/9812765).
14. Nathan, R.J.A.A.; Kurmi, I.; Bimber, O. Inverse Airborne Optical Sectioning. *Drones* **2022**, *6*, 231, doi:[10.3390/drones6090231](https://doi.org/10.3390/drones6090231).
15. Nathan, R.J.A.A.; Kurmi, I.; Bimber, O. Drone Swarm Strategy for the Detection and Tracking of Occluded Targets in Complex Environments. *Commun Eng* **2023**, *2*, 1–12, doi:[10.1038/s44172-023-00104-0](https://doi.org/10.1038/s44172-023-00104-0).
16. Seits, F.; Kurmi, I.; Bimber, O. Evaluation of Color Anomaly Detection in Multispectral Images for Synthetic Aperture Sensing. *Eng* **2022**, *3*, 541–553, doi:[10.3390/eng3040038](https://doi.org/10.3390/eng3040038).
17. Nathan, R.J.A.A.; Bimber, O. Synthetic Aperture Anomaly Imaging for Through-Foliage Target Detection. *Remote Sensing* **2023**, *15*, 4369, doi:[10.3390/rs15184369](https://doi.org/10.3390/rs15184369).
18. Li, S.; Yang, B.; Hu, J. Performance Comparison of Different Multi-Resolution Transforms for Image Fusion. *Information Fusion* **2011**, *12*, 74–84, doi:[10.1016/j.inffus.2010.03.002](https://doi.org/10.1016/j.inffus.2010.03.002).
19. Cao, L.; Jin, L.; Tao, H.; Li, G.; Zhuang, Z.; Zhang, Y. Multi-Focus Image Fusion Based on Spatial Frequency in Discrete Cosine Transform Domain. *IEEE Signal Processing Letters* **2015**, *22*, 220–224, doi:[10.1109/LSP.2014.2354534](https://doi.org/10.1109/LSP.2014.2354534).
20. Chen, J.; Li, X.; Luo, L.; Mei, X.; Ma, J. Infrared and Visible Image Fusion Based on Target-Enhanced Multiscale Transform Decomposition. *Information Sciences* **2020**, *508*, 64–78, doi:[10.1016/j.ins.2019.08.066](https://doi.org/10.1016/j.ins.2019.08.066).
21. Awad, M.; Elliethy, A.; Aly, H.A. Adaptive Near-Infrared and Visible Fusion for Fast Image Enhancement. *IEEE Transactions on Computational Imaging* **2020**, *6*, 408–418, doi:[10.1109/TCI.2019.2956873](https://doi.org/10.1109/TCI.2019.2956873).
22. Li, H.; Wu, X.-J. Multi-Focus Image Fusion Using Dictionary Learning and Low-Rank Representation. In *Proceedings of the Image and Graphics*; Zhao, Y., Kong, X., Taubman, D., Eds.; Springer International Publishing: Cham, 2017; pp. 675–686.
23. Li, H.; Wu, X.-J.; Kittler, J. MDLatLRR: A Novel Decomposition Method for Infrared and Visible Image Fusion. *IEEE Transactions on Image Processing* **2020**, *29*, 4733–4746, doi:[10.1109/TIP.2020.2975984](https://doi.org/10.1109/TIP.2020.2975984).
24. Li, H.; Wu, X.-J.; Kittler, J. Infrared and Visible Image Fusion Using a Deep Learning Framework. In *Proceedings of the 2018 24th International Conference on Pattern Recognition (ICPR)*; August 2018; pp. 2705–2710.
25. Hou, R.; Zhou, D.; Nie, R.; Liu, D.; Xiong, L.; Guo, Y.; Yu, C. VIF-Net: An Unsupervised Framework for Infrared and Visible Image Fusion. *IEEE Transactions on Computational Imaging* **2020**, *6*, 640–651, doi:[10.1109/TCI.2020.2965304](https://doi.org/10.1109/TCI.2020.2965304).
26. Jian, L.; Yang, X.; Liu, Z.; Jeon, G.; Gao, M.; Chisholm, D. SEDRFuse: A Symmetric Encoder–Decoder With Residual Block Network for Infrared and Visible Image Fusion. *IEEE Transactions on Instrumentation and Measurement* **2021**, *70*, 1–15, doi:[10.1109/TIM.2020.3022438](https://doi.org/10.1109/TIM.2020.3022438).
27. Zhao, W.; Xie, S.; Zhao, F.; He, Y.; Lu, H. MetaFusion: Infrared and Visible Image Fusion via Meta-Feature Embedding From Object Detection. In *Proceedings of the IEEE/CVF Conference on Computer Vision and Pattern Recognition*; 2023; pp. 13955–13965.



28. Li, H.; Wu, X.-J.; Kittler, J. RFN-Nest: An End-to-End Residual Fusion Network for Infrared and Visible Images. *Information Fusion* **2021**, *73*, 72–86, doi:[10.1016/j.inffus.2021.02.023](https://doi.org/10.1016/j.inffus.2021.02.023).
29. Xu, H.; Zhang, H.; Ma, J. Classification Saliency-Based Rule for Visible and Infrared Image Fusion. *IEEE Transactions on Computational Imaging* **2021**, *7*, 824–836, doi:[10.1109/TCI.2021.3100986](https://doi.org/10.1109/TCI.2021.3100986).
30. Park, S.; Vien, A.G.; Lee, C. Cross-Modal Transformers for Infrared and Visible Image Fusion. *IEEE Transactions on Circuits and Systems for Video Technology* **2023**, 1–1, doi:[10.1109/TCSVT.2023.3289170](https://doi.org/10.1109/TCSVT.2023.3289170).
31. Ma, J.; Tang, L.; Fan, F.; Huang, J.; Mei, X.; Ma, Y. SwinFusion: Cross-Domain Long-Range Learning for General Image Fusion via Swin Transformer. *IEEE/CAA Journal of Automatica Sinica* **2022**, *9*, 1200–1217, doi:[10.1109/JAS.2022.105686](https://doi.org/10.1109/JAS.2022.105686).
32. Liu, J.; Lin, R.; Wu, G.; Liu, R.; Luo, Z.; Fan, X. CoCoNet: Coupled Contrastive Learning Network with Multi-level Feature Ensemble for Multi-modality Image Fusion. *International Journal of Computer Vision (IJCV)*, 2023 (to appear).
33. Vaswani, A.; Shazeer, N.; Parmar, N.; Uszkoreit, J.; Jones, L.; Gomez, A.N.; Kaiser, Ł.; Polosukhin, I. Attention Is All You Need. In *Proceedings of the Advances in Neural Information Processing Systems*; Curran Associates, Inc., 2017; Vol. 30.
34. Goodfellow, I.; Pouget-Abadie, J.; Mirza, M.; Xu, B.; Warde-Farley, D.; Ozair, S.; Courville, A.; Bengio, Y. Generative Adversarial Nets. In *Proceedings of the Advances in Neural Information Processing Systems*; Curran Associates, Inc., 2014; Vol. 27.
35. Ma, J.; Yu, W.; Liang, P.; Li, C.; Jiang, J. FusionGAN: A Generative Adversarial Network for Infrared and Visible Image Fusion. *Information Fusion* **2019**, *48*, 11–26, doi:[10.1016/j.inffus.2018.09.004](https://doi.org/10.1016/j.inffus.2018.09.004).
36. Zhang, H.; Yuan, J.; Tian, X.; Ma, J. GAN-FM: Infrared and Visible Image Fusion Using GAN With Full-Scale Skip Connection and Dual Markovian Discriminators. *IEEE Transactions on Computational Imaging* **2021**, *7*, 1134–1147, doi:[10.1109/TCI.2021.3119954](https://doi.org/10.1109/TCI.2021.3119954).
37. Ma, J.; Xu, H.; Jiang, J.; Mei, X.; Zhang, X.-P. DDcGAN: A Dual-Discriminator Conditional Generative Adversarial Network for Multi-Resolution Image Fusion. *IEEE Transactions on Image Processing* **2020**, *29*, 4980–4995, doi:[10.1109/TIP.2020.2977573](https://doi.org/10.1109/TIP.2020.2977573).
38. Li, S.; Kang, X.; Hu, J. Image Fusion With Guided Filtering. *IEEE Transactions on Image Processing* **2013**, *22*, 2864–2875, doi:[10.1109/TIP.2013.2244222](https://doi.org/10.1109/TIP.2013.2244222).
39. Simonyan, K.; Zisserman, A. Very Deep Convolutional Networks for Large-Scale Image Recognition. *arXiv* **2014**, *arXiv preprint arXiv:1409.1556*.
40. Liu, J.; Fan, X.; Huang, Z.; Wu, G.; Liu, R.; Zhong, W.; Luo, Z. Target-Aware Dual Adversarial Learning and a Multi-Scenario Multi-Modality Benchmark To Fuse Infrared and Visible for Object Detection. In *Proceedings of the IEEE/CVF Conference on Computer Vision and Pattern Recognition*, 2022, pp 5802–5811.
41. Toet, A. The TNO Multiband Image Data Collection. *Data in Brief* **2017**, *15*, 249–251, doi:[10.1016/j.dib.2017.09.038](https://doi.org/10.1016/j.dib.2017.09.038).